Nano Energy 76 (2020) 104926

Contents lists available at ScienceDirect

Nano Energy

journal homepage: http://www.elsevier.com/locate/nanoen

Soft bimorph actuator with real-time multiplex motion perception

Hongtao Zhao [a,1], Run Hu [b,1], Pan Li [c], Anzhu Gao [d], Xuantong Sun [e], Xiaohui Zhang [a], Xiangjun Qi [a], Qiang Fan [a], Yida Liu [b], Xuqing Liu [e], Mingwei Tian [a,**], Guangming Tao [c,*], Lijun Qu [a,f,***]

[a] Research Center for Intelligent and Wearable Technology, College of Textiles and Clothing, State Key Laboratory of Bio-Fibers and Eco-Textiles, Qingdao University, Qingdao, 266071, PR China
[b] State Key Laboratory of Coal Combustion and School of Energy and Power Engineering, Huazhong University of Science and Technology, Wuhan, 430074, PR China
[c] Wuhan National Laboratory for Optoelectronics and School of Optical and Electronic Information, Huazhong University of Science and Technology, Wuhan, 430074, PR China
[d] Institute of Medical Robotics and Department of Automation, Shanghai Jiao Tong University, Key Laboratory of System Control and Information Processing, Ministry of Education, Shanghai, 200240, PR China
[e] University of Manchester, School of Materials, Oxford Road, Manchester, M13 9PL, Lancs, England, UK
[f] Jiangsu College of Engineering and Technology, Nantong, Jiangsu, 226007, PR China

ARTICLE INFO

Keywords:
Motion perception
Soft actuator
Self-sensing
Thermochromic
Multiplexing

ABSTRACT

Soft actuators with accurate and real-time motion perception are of great importance for flexible machines and artificial intelligence robotics to enable an autonomic response to surroundings. To enhance the sensing-signal reliability and calibration, synchronous motion perception with multiplex feedback signals is desired but has not been sufficiently explored. Herein, we present a soft bimorph actuator that has electrical and visual dual channel signal feedback functions for real-time multiplex motion perception. Cellulose paper and polyimide tape were assembled together as bimorph actuation layers on which an MXene/graphene bilayer was coated for electrothermal function and electrical signal feedback and a thermochromic interlayer was used for real-time visual signal feedback. Based on the proposed actuators, three kinds of bionic robotics and an electro-puppetry robot, "*Wu Song Fights the Tiger*", with motion-programmable features are demonstrated, revealing the broad application prospects of the present soft actuators in bionic soft robotics with real-time multiplexing motion perception.

1. Introduction

The most recent decade has witnessed a surging development in soft actuators, largely in compliance and promotion of the rapid development of flexible machines and artificial intelligence (AI) robotics. During this effort, a number of intriguing and potential applications have been reported, such as artificial muscles, bionic robotics, skin-like sensors, smart textiles, multifunctional fibres, and bio-medicine [1–12]. These soft actuators are usually capable of self-deformation under external stimuli such as electrics [13–15], light [16–18], heat [19–21], moisture [22–24], and magnetics [25–27]. To obtain both short-term soft actuators and long-term AI robotics, accurate real-time motion perception under external stimuli is essential in actuators, robotics and intelligent autonomous systems. Most of these soft actuators are rather small, compact, and integrated but cannot resort to external sensors and computers to achieve their motion perception due to limitations in space and power supply. Hence, the integration of self-sensing function is the development tendency of the new generation of soft actuator which can feedback its motion state without additional sensors. These soft actuators are also desired as good sensors that can detect, measure, and perceive motion (self-sensing) in real time and would be even more preferably if they simultaneously perceive the motion in multiple ways.

* Corresponding author.
** Corresponding author.
*** Corresponding author. Research Center for Intelligent and Wearable Technology, College of Textiles and Clothing, State Key Laboratory of Bio-Fibers and Eco-Textiles, Qingdao University, Qingdao, 266071, PR China.
E-mail addresses: mwtian@qdu.edu.cn (M. Tian), tao@hust.edu.cn (G. Tao), lijunqu@qdu.edu.cn (L. Qu).
[1] These authors contributed equally to this work.

https://doi.org/10.1016/j.nanoen.2020.104926
Received 4 April 2020; Received in revised form 26 April 2020; Accepted 2 May 2020
Available online 26 June 2020

However, the existing soft actuators can only sense by electrical signals such as current, resistance and capacitance. This single signal feedback mode is prone to deviates in a complex work environment. Multiplex real-time motion perception has thus far remained poorly explored but has attracted increasing attention in recent years for enhancing the reliability and calibration of multiplex motion perception signals.

Electrical signal feedback is the most widely used route for motion perception of soft actuators, and recently, a few studies have attempted self-sensing by detecting real-time resistance changes [5,28]. For thermal-driven soft bimorph actuators, a self-sensing function can be achieved via temperature-independent piezoresistive properties, i.e., the conductive layer of the actuator must possess a low temperature coefficient of resistance (TCR) in the applied temperature range. Low-TCR conductive materials can be synthesized from two conductive materials with opposite resistance-temperature characteristics (e.g., MXene, with a positive TCR, and graphene, with a negative TCR) [29–31]. In addition to electrical signal feedback, visual signal feedback is a convenient way for humans to easily and visually detect actuating behaviors. Finally, visual signals are much easier to perceive by human eyes when allochromatic materials (including electrochromic [32], thermochromic [33] and photochromic [34]) with enhanced discrimination of colour change under external stimuli are used; among these stimuli, heat is the most conventional and general driving stimulus without an additional power supply.

Further elaborating on recent progress in robot motion perception by electrical and visual signal feedback, we present a thermal/electrothermal-driven soft bimorph actuator with thermochromic and self-sensing dual functionalities for multiplex real-time motion perception. The soft actuator is fabricated by taking commercial cellulose paper and polyimide (PI) tape as deformation substrates. An MXene/graphene (M/G) bilayer with low TCR and high piezoresistivity is coated on cellulose paper to endow electrothermal and self-sensing properties. A specially designed thermochromic material, zinc-ion-intercalated layered polydiacetylene (PDA-Zn^{2+}), is synthesized in situ on a cellulose paper substrate with good intuitive colour-change capability for real-time visual signal feedback at the wide temperature range of 40–140 °C. Three kinds of bionic robotics are assembled based on soft actuators: a lightweight claw, an artificial tactile finger and a walking, colourful inchworm. In addition, by integrating the soft actuators into Chinese shadow puppetry, we developed an electro-puppetry robot "*Wu Song Fights the Tiger*" with motion-programmable features, revealing the broad application prospects of the present soft actuators in bionic soft robotics and their great potential in highly robust, multiplex motion perception.

2. Experimental section

2.1. Preparation of T-paper

Thermochromic paper (T-paper) was prepared through crystal growth, intercalation, and topochemical polymerization. In detail, a commercial cellulose paper (70 g/m^2) was dipped in 10 ml dichloromethane solution (CH_2Cl_2, Aladdin, 99.5%) containing 0.1 g 10,12-pentacosadiynoic acid (PCDA, Aladdin, 97%) in a Petri dish for 5 s, and PCDA-coated paper was obtained after the solvent evaporated completely. Then, the PCDA-coated paper was immersed in 10 ml 5 vol % tetrahydrofuran (THF, Aladdin, 99.5%) aqueous solution containing 0.05 g zinc acetate dihydrate ($C_4H_6O_4Zn{\bullet}2H_2O$, Aladdin, 99.0%) for 24 h at 25 °C. The obtained paper coated with Zn^{2+}-intercalated PCDA (PCDA-Zn^{2+}) was washed with purified water and then dried at room temperature. The thermochromic paper was prepared through irradiation of UV light for 30 min at a temperature of 20 °C. The polymerization of PCDA-Zn^{2+} was carried out through an ultraviolet lamp (CHF-XM500, 500 W) with wavelength of 256 nm, and the work distance was set at 200 mm to prevent local temperature from being too high.

2.2. Preparation of TSA

The TSA was fabricated by attaching a PI adhesive tape to T-paper.

2.3. Preparation of ETS-paper

The preparation of ETS-paper consists of two steps. In the first step, the T-paper substrate was sprayed with MXene solution (2 mg/mL) and dried at room temperature. Subsequently, an M/G bilayer was constructed by spraying the graphene solution (2 mg/mL) on the MXene layer. The spray coating was carried out according to previous studies [35,36], and the parameters spraying pressure, fluid flux and time were set at 0.5 MPa, 0.5 mL/cm^2 and 5 s, respectively.

2.4. Preparation of the ETSA

The ETSA was prepared by attaching a PI adhesive tape to ETS-paper.

2.5. Characterization

Micro-structures of the samples were characterized via SEM (EHT, ZEISS EVO18, 3.0 kV; work distance, 8.0 mm). Temperature distributions of all samples were obtained via an IR camera (FLIR systems, A645sc). Emission light intensity and chromaticity coordinates were measured with a Photoresearch PR-655.

Actuator samples were obtained by tailoring a TSA or an ETSA into a strip (40 × 15 mm). For TSAs, a modified oven was used to provide a constant heat source for actuation testing. For ETSAs, a DC voltage was applied via a System Source Meter (Keithley 2601B). The deformation performance of the actuator sample is expressed by its curvature. The curvature of the sample can be obtained by an iterative algorithm according to the following formula:

$$r_{n+1} = (1 + \frac{l - 2{\cdot}r_n{\cdot}\sin(c/(2{\cdot}r_n))}{l - c{\cdot}\cos(c/(2{\cdot}r_n))}){\cdot}r_n \quad (1)$$

where r is the radius of curvature, n is the iteration number, l is the arc length of the actuators, and c is the chord length of the actuators.

The dynamic resistance in the TCR test, sensing test and self-sensing test was determined using a System Source Meter (Keithley 2601B). A homemade thruster with a servo motor was used to tension or compress samples. The bending strain of samples can be obtained by

$$\varepsilon = \pm h/r \quad (2)$$

where ε is the bending strain of actuators, h is the distance of conductive films from the neutral axis of the bimorph structure (~95.65 μm, see Fig. S1, Supporting Information), and r is the radius of curvature. In addition, the sensitivity (GF value) of the samples under different strain conditions was calculated as

$$GF = \frac{\Delta R/R_0}{\varepsilon} \quad (3)$$

where GF is the sensitivity of the actuators, ΔR is the resistance change (Ω), R_0 is the initial resistance (Ω), and ε is the bending strain.

3. Results and discussion

3.1. Design and fabrication of actuators

The fabrication process of the soft bimorph actuator is illustrated in Fig. 1a. Here, commercial cellulose paper is chosen as the base material and then decorated with PDA-Zn^{2+} through crystal growth, intercalation, and topochemical polymerization to obtain thermochromic paper (T-paper) (Fig. S2, Supporting Information) [37]. The key of the thermal-driven bimorph actuator primarily lies in the thermal expansion properties of the two substrate layers. Polyimide (PI) tape is selected as

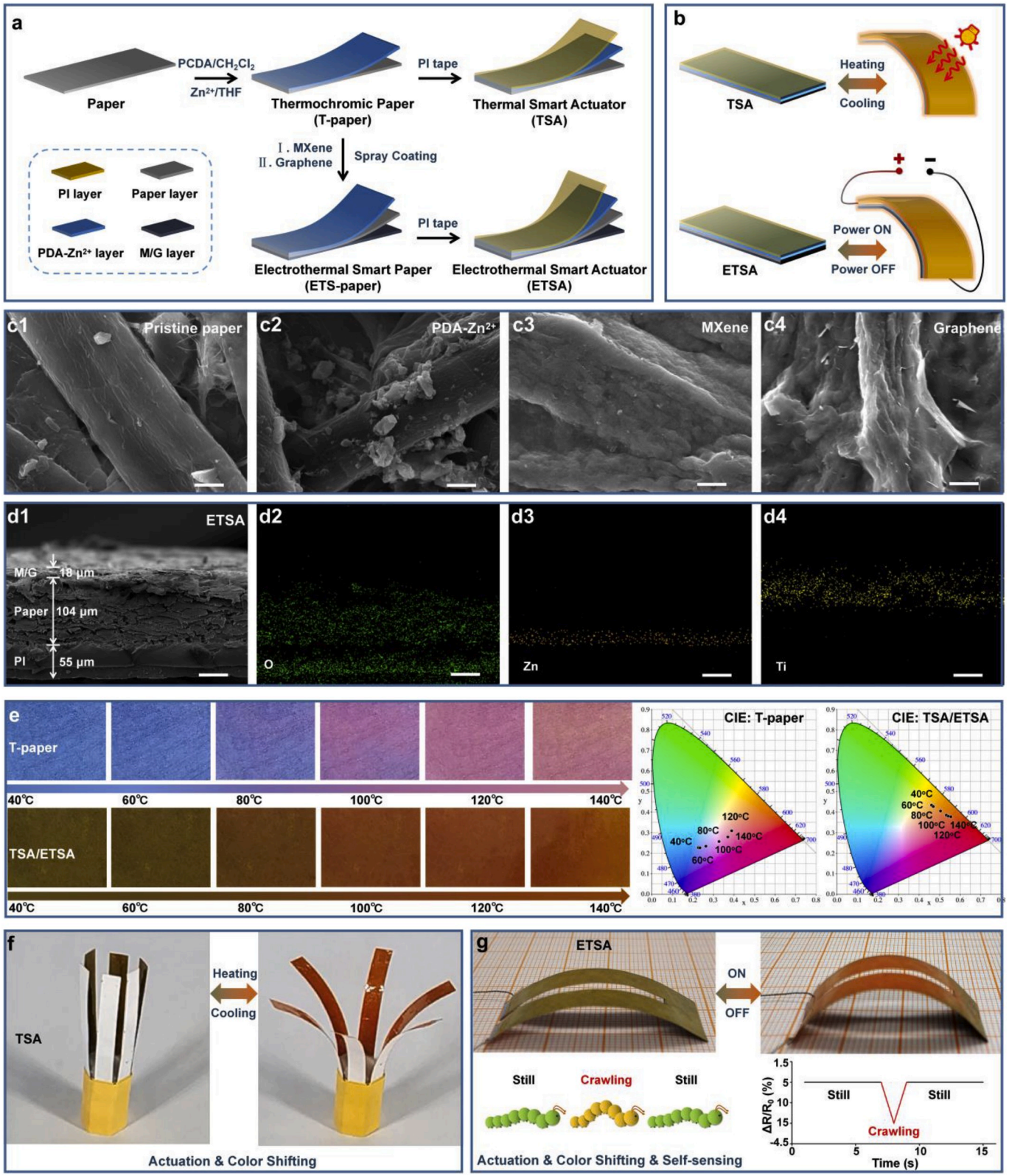

Fig. 1. Fabrication and characterization of the bimorph TSAs and ETSAs. (a) Schematic illustration of the fabrication process of the TSA and ETSA. (b) Actuation schematic diagrams of the TSA and ETSA. (c) Morphology evolution from pristine paper to an ETSA: 1. Pristine paper; 2. Crystalline PDA-Zn^{2+} decorated on cellulose fibre; 3. MXene coated on cellulose fibre; 4. Graphene coated on Mxene. Scale bars 5 μm. (d) Morphology characterization of an ETSA: 1 Cross-sectional SEM image of the ETSA; 2–4 An EDX image depicting the distribution of cross-sectional O, Zn and Ti elements of the ETSA. Scale bars 50 μm. (e) Optical photos and International Commission on Illumination (CIE) colour coordinate diagrams of T-paper and an ETSA at temperatures from 40 °C to 140 °C. (f) TSA-based thermochromic artificial flower shifting colour during heating and cooling. (g) ETSA-based walking, colourful inchworms with both colour shifting and motion state monitoring.

the active layer due to its high coefficient of thermal expansion (CTE) and low coefficient of hygroscopic expansion (CHE); meanwhile, cellulose paper is chosen as the passive layer for its isotropic low CTE and high CHE. To achieve a bimorph structure, a thermal soft actuator (TSA) and an electrothermal soft actuator (ETSA) are fabricated. The TSA is feasibly obtained by attaching PI tape onto the T-paper. The TSA can be directly driven by temperature changes. To obtain the ETSA, an M/G bilayer is coated on the T-paper first to prepare ETS-paper by a layer-by-layer spraying method and then adhered to PI tape. The ETSA can be driven by a certain DC voltage, generating Joule heat (Fig. 1b).

The surface and cross-section morphology of the actuators are illustrated in Fig. 1c and d, respectively. After the in situ synthesis of PDA-Zn^{2+}, crystalline particles are deposited on the surface of fibrous paper, which tends to be frosted after being sprayed with an MXene microlayer and then evolved to wrinkle when covered with a graphene microlayer. The ETSA exhibits a classical laminated micro-structure with the stacking of an M/G bilayer (~18 μm) on the surface of the paper layer (~104 μm). Furthermore, the corresponding energy-dispersive X-ray (EDX) maps of every layer also exhibit stacking. The Ti element of MXene and Zn element of PDA-Zn^{2+} are both distributed wider than those in scanning electron microscopy (SEM) images, which might be caused by penetration of MXene and PDA-Zn^{2+} into the paper, reflecting a good interface between the inside layers.

When the temperature increases from 40 to 140 °C, the T-paper exhibits a reversible thermochromic response with an obvious colour shift from blue to red, and the TSA (ETSA) accordingly demonstrates a colour change from tea green to orange-red. Meanwhile, the chromaticity coordinates of T-paper (x, y) change from (0.23, 0.23) to (0.39, 0.31), and for TSA (ETSA), they change from (0.46, 0.43) to (0.55, 0.38), as illustrated in Fig. 1e. Therefore, the resultant TSA and ETSA based on the T-paper both show reasonable actuating behaviour with additional self-sensing visual signal feedback. For example, an artificial flower composed of six serially connected TSA units as petals and exposed to high temperature at 120 °C can gradually bloom with TSA petals self-bending outward and simultaneously colour shifting from tea green to orange-red (Fig. 1f). Moreover, inspired by the movement of worms, we prepare a walking, colourful inchworm based on the ETSA that not only exhibits visual feedback of temperature by colour shifting but also monitors its motion state by a resistance signal during crawling, as shown in Fig. 1g.

3.2. TSA deformation and thermochromic characterization

The deformation performance and visual thermochromic response of the TSA were investigated (Fig. 2). After the TSA is put on a heating plate for 20 s, its actuating procedure is recorded as in Fig. 2a. The curvature of the actuator shows an increasing tendency with increasing setting temperature from 70 °C to 130 °C. At 130 °C, the curvature reaches ~1 cm^{-1} in 20 s. Such an obvious deformation can be explained by asymmetric expansion/shrinkage of the PI/paper bimorph structure of the TSA, as shown in Fig. 2b. PI molecular chains, especially in the amorphous region, are activated and expanded under high temperature, leading to expansion of the PI layer [38]. However, evaporation of the water molecules in the cellulose paper results in the shrinkage of the paper layer [5]. The opposite deformation generates warping, which is the working principle of the TSA.

The TSA exhibits a visual thermochromic response along with deformation, gradually shifting from tea green to orange-red with increasing temperature (Fig. 2c). Within 6000 heating-cooling cycles, the maximum curvature of the actuator always fluctuates approximately 1 cm^{-1}, and the thermochromism of the actuator shows marginal deterioration (Fig. 2d), revealing a predictable long and stable working life. As a proof-of-concept, we fabricated an artificial flower based on using the TSA as petals to vividly demonstrate simultaneous blooming deformation and colour shifting (Fig. 2e). When exposed to high temperature (an oven at 120 °C), the petals bend outward from the centre, and their colour changed from tea green to orange-red (Movie S1, Supporting Information). IR images show a gradual change in temperature.

Supplementary video related to this article can be found at https://doi.org/10.1016/j.nanoen.2020.104926

Such TSA characterization builds our confidence that the deformation can be perceived by the visual feedback of colour shifting and inspires us to develop an ETSA as the advanced version of the TSA for integration with electrical signal sensing capability.

3.3. ETSA TCR and thermochromic characterization

The TCR is a key index to characterize the resistance dependence of conductive materials on the temperature, which is especially critical to electrothermal actuators integrated with a self-sensing function [29]. Here, positive-TCR (PTC) MXene and negative-TCR (NTC) graphene are chosen as the substrates to prepare a low-TCR conductive bilayer by optimizing their wight ratio (see Fig. S3 for details, Supporting Information). Fig. 3a shows the relative resistance changes in an MXene film, a graphene film and an M/G bilayer under different temperatures. It is shown that the relative resistance and TCR of MXene and graphene are completely opposite. That's because increase in inelastic electron scattering and lattice spacing with temperature, MXene films exhibit PTC similar to metals, while graphene films exhibit NTC ascribed to more hot carriers produced by increasing temperature [39,40]. In details, when the temperature increases from 40 to 180 °C, the relative resistance in the MXene film and graphene film varies by 30.78% and −14.14%, respectively, while that of the M/G bilayer decreases significantly. In particular, the M/G bilayer with a weight ratio of 1:2.5 exhibits the lowest relative resistance changes (<0.5%), which is the best case with a sufficiently low TCR. Correspondingly, as illustrated in Fig. 3b, the absolute value of the average TCR of M/G-1:2.5 is reduced to less than $8 \times 10^{-5}\ K^{-1}$ in the temperature range of 40–180 °C, which is far lower than that of pristine MXene film ($2.41 \times 10^{-3}\ K^{-1}$) or graphene film ($1.78 \times 10^{-3}\ K^{-1}$). Therefore, M/G-1:2.5 is employed to fabricate the ETSA in this work.

To analyse the electrothermal performance of the ETSA, a heater with dimensions of 40 × 15 mm is prepared by proper tailoring. Fig. 3c presents the time-dependent temperature profiles of the heater at different voltages. The ETSA temperature increases rapidly after the voltage is turned on and reaches a steady temperature; it then drops rapidly to room temperature after the voltage is turned off. It takes only approximately 10 s to heat up to the steady temperature (168 °C at 12 V) or to cool to room temperature (13.56 °C/s), which is much faster than the graphene-based heater in our previous reports [41–43]. This excellent electrothermal effect benefits from the low resistance and high electrothermal conversion performance of MXene [44,45]. In addition, with 10 V as an example, margin deterioration in the electrothermal performance of the ETSA is observed in 20 cycles (Fig. 3d), revealing its good reliability and stability. Furthermore, the effect of the electrothermal performance of the ETSA on its thermochromism is also investigated. The temperature of the ETSA rises from ~39 °C (4 V) to ~168 °C (12 V), and the colour of the ETSA correspondingly changes from tea green to orange-red (Fig. 3e) with a short delay time (Fig. S4, Supporting Information), revealing as good a thermochromic performance as the previous TSA. Therefore, we can obtain the real-time temperature by observing the colour of the ETSA without an extra thermometer.

3.4. ETSA deformation and sensing

The sensing response of the ETSA is evaluated and illustrated in Fig. 4a. The relative resistance changes ($\Delta R/R_0$) exhibit opposite responses under tension and compression deformations, but the relative resistance changes in the ETSA show similarly increasing dependences when the deformation is increased from ε 0.4%–0.8%. This relative resistance change trend can be explained by connection and

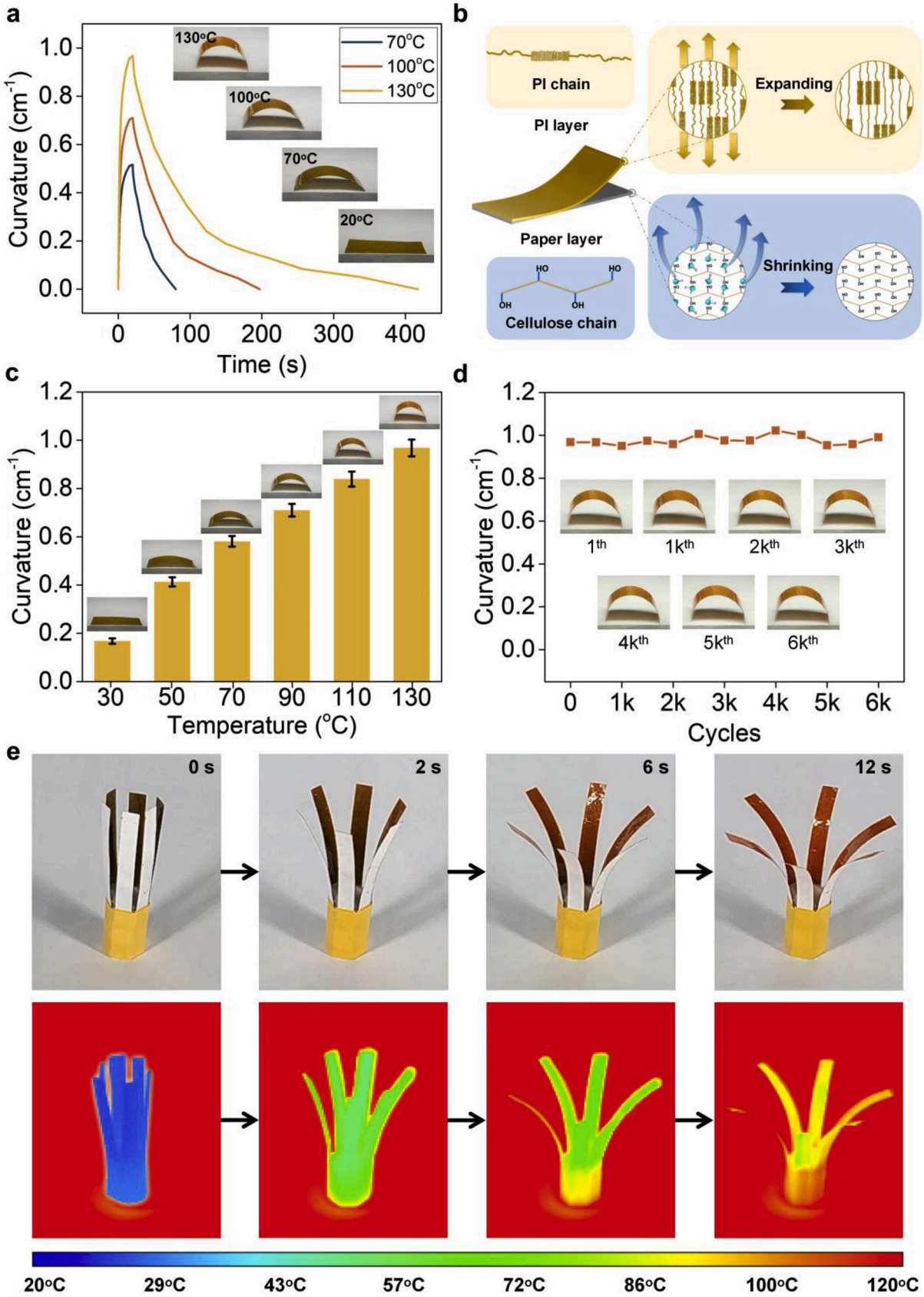

Fig. 2. TSA thermal-driven deformation and colour-shifting characterization. (a) TSA curvature change at different temperatures. (b) The actuation mechanism of the TSA. (c) Maximum curvature of the TSA at different temperatures. Insets: colour change in the TSA at different temperatures. (d) Cyclic stability of the TSA in terms of the maximum curvature. (e) Bionic colour-shifting flower composed of the TSA with increasing temperature.

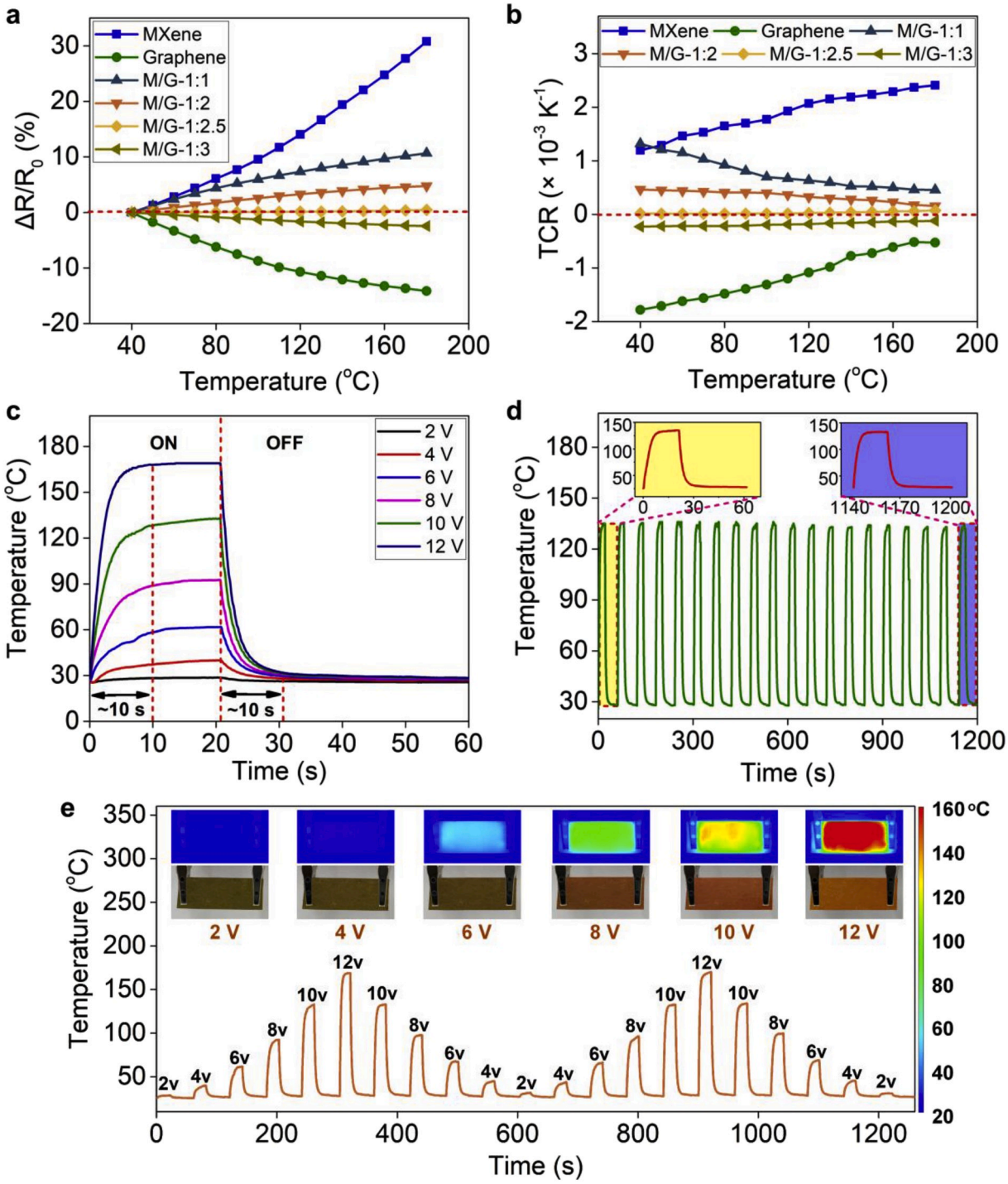

Fig. 3. ETSA electrically driven TCR and thermochromic characterization. (a) Relative resistance and (b) average TCR of an MXene film, a graphene film and an M/G bilayer at different temperatures. (c) Electrothermal characterization of the ETSA heater under different applied voltages. (d) Cyclic heating of the ETSA under an applied voltage of 10 V. (e) Temperature response of the ETSA to a series of stepped applied voltages. Insets: IR and optical pictures of the ETSA under different applied voltages.

disconnection of graphene sheets and MXene sheets [5,46–48]. As depicted in Fig. 4b, when the ETSA is tensioned, induced stretching in the M/G bilayer reduces the overlapped area and junctions where graphene and MXene are connected, while when the ETSA is compressed, the overlapped area and junctions increase, which gives rise to the opposite response in the relative resistance change shown in Fig. 4a.

To quantitatively analyse the sensing performance of the ETSA, we derive and analyse the relationship between the relative resistance and the bending strain (see the Materials and Methods for details). The gauge factor (GF) values of the ETSA under compression and tension are measured to be 15.34 and 11.1, respectively (Fig. 4c), implying that the sensing behaviour of the ETSA is more sensitive under compression strain than under tension strain. Coupling this difference with a higher linear piezoresistive response ($R^2 = 0.96$) under compression strain indicates that the ETSA can be used for compression strain sensing applications. Additional tests are conducted to further investigate the resistance response of a sample to a series of stepped strain (−0.2%, −0.4%, −0.6% and −0.8%) loading cycles (Fig. 4d). The ETSA

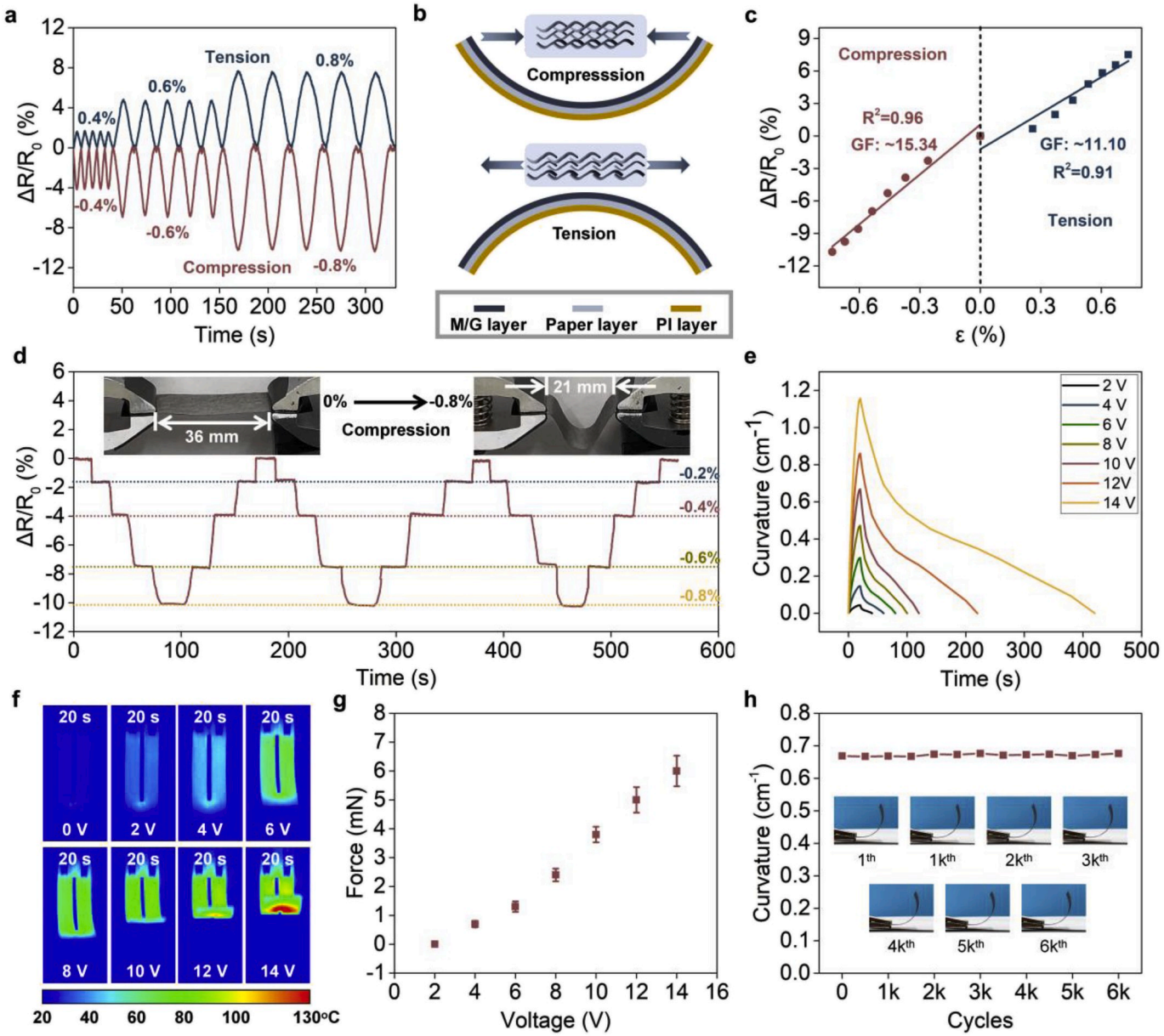

Fig. 4. ETSA deformation sensing characterization. (a) Resistance response of an ETSA to tension and compression. (b) Schematic diagram of tension and compression tests for a sensing evaluation of the ETSA. (c) Relative resistance versus tension and compression strain for the ETSA. (d) Relative resistance response of the ETSA to cyclic stepwise compression loading. Insets: optical images of the actuator at straight and compression states. (e) The curvature of the ETSA versus time under different applied voltages. (f) IR images of the ETSA under different voltages after 20 s of power on. (g) Blocking force under different applied voltages. (h) Cyclic stability of the ETSA.

sensitively detects relative resistance changes under different bending strains and possesses satisfactory cycle life with robust and stable output of electrical signals.

To investigate the actuation performance of ETSA, a U-shaped ETSA is fabricated (Fig. S5, Supporting Information) and analysed considering its curvature and blocking force. Upon the application of a DC voltage, the ETSA reaches its maximum curvature in ~20 s. The maximum curvature of the ETSA increases with increasing applied voltage and reaches 1.15 cm^{-1} under 14 V (Fig. 4e). The IR images in Fig. 4f show the colour shifting from blue to red, corresponding to the rising temperature with increasing applied voltage and curvature. Therefore, the ETSA deformation is also reflected in its temperature due to the quick thermochromic response. As shown in Fig. 4g, the maximum blocking force of the ETSA increases with increasing applied voltage. In particular, when the applied voltage is 14 V, the ETSA generates ~6 mN of blocking force.

In addition, the cyclic stability of the ETSA is also investigated by taking 10 V of applied voltage as an example. As shown in Fig. 4h, the maximum curvature of the ETSA remains ~0.67 cm^{-1} for 6000 cycles, demonstrating a robust and stable cycle life.

3.5. Motion perception via electrical and visual signal feedback

Since ETSAs, as the advanced versions of TSAs, can be driven by both heat and electricity with excellent quick, sensitive, stable, and robust electrothermal and self-sensing performances, we apply it as a soft actuator and self-sensor to move while monitoring the motion through its output electrical and visual signals. As shown in Fig. 5a, when the power is on, the curvature of the ETSA gradually increases while its relative resistance decreases correspondingly. When the power is off, the relative resistance of the ETSA gradually returns to zero while the

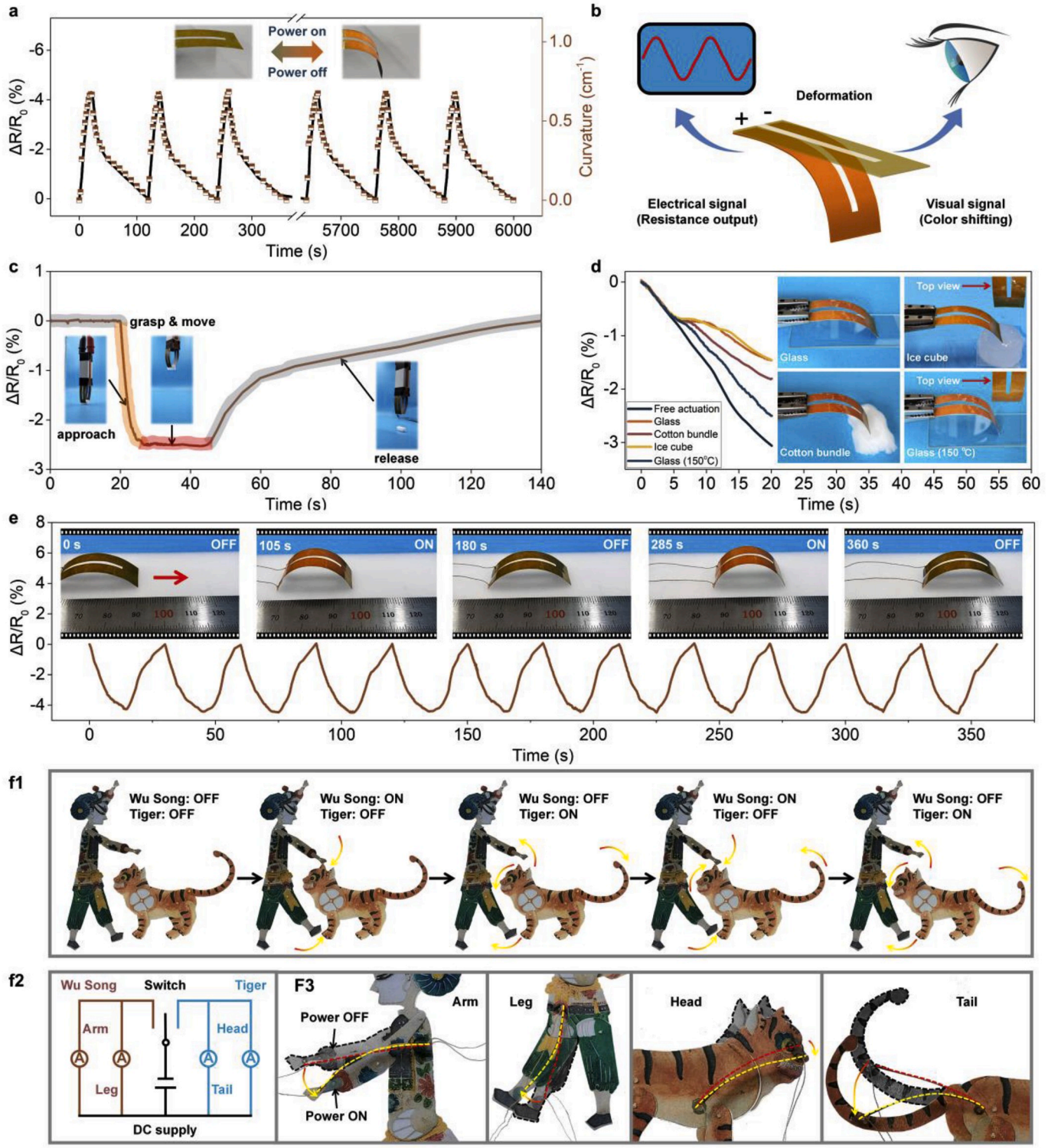

Fig. 5. Motion perception by ETSAs with electrical and visual signal feedback. (a) Self-sensing performance of the ETSA. Insets: bending deformation of the ETSA under 10 V of applied voltage. (b) Schematic illustrating that the ETSA can feedback electrical and visual signals in real time while deforming. (c) Sensory response of the smart lightweight claw grasping and releasing a sponge. Insets: optical photos of the smart lightweight claw approaching, grasping, moving and releasing the sponge. (d) Relative resistance of the artificial tactile finger freely actuating and touching different objects. Insets: optical images of the artificial tactile finger touching different objects. (e) Relative resistance response during crawling of the walking colourful inchworm. Insets: optical photos of the walking, colourful inchworm at different stages of crawling. (f) The ETSA was used in the Chinese traditional shadow play *Wu Song Fights the Tiger*. 1: freeze frames of *Wu Song Fights the Tiger*, 2: diagram of control circuit, 3: actuation diagrams of arm, leg, head and tail.

deformation disappears gradually. The curvature and relative resistance show similar trends with negligible fluctuations in 50 cycles, demonstrating the expected robust and stable self-sensing capability. In addition, the ETSA exhibits a real-time colour response (from tea green to orange-red) while deforming, as shown in the insets. Thus, unlike previous soft actuators, the present soft actuator can feedback electrical and visual signals in real time while undergoing motion without additional measuring tools (Fig. 5b), which provides additional possibilities for the application of actuators in smart bionics.

To demonstrate the application of the ETSA in bionic robotics, a smart lightweight claw consisting of two U-shaped ETSAs is fabricated, and a grabbing sponge experiment is carried out (Movie S2, Supporting Information). The output resistance and optical images at different steps in grasping a sponge block are illustrated in Fig. 5c. In the beginning, the two ETSAs of the claw are parallel and straight. Once a DC voltage (12 V) is applied, the tips of the claw gradually deform and draw close to each other, and the relative resistance of the claw decreases rapidly until the sponge block is grasped. Then, we use the claw to hold the sponge and move, and the corresponding relative resistance remains stable. Finally, when powered off, the claw releases the sponge block, its relative resistance gradually returns to 0, and the claw returns to the original parallel and straight state. This smart lightweight claw experiment demonstrates the perfect integration of grasping actuation and real-time motion perception.

Supplementary video related to this article can be found at https://doi.org/10.1016/j.nanoen.2020.104926

Since the signal feedback of the ETSA is based on deformation and temperature, the soft actuator can also be used as an artificial tactile finger to touch and recognize objects (Fig. 5d). The relative resistance of the finger constantly decreases while bending until the finger touches a piece of glass, an ice cube, and a soft cotton bundle; then, its relative resistance decreases slowly since further deformation is confined by the objects. Compared to touching glass and ice cubes, touching the soft cotton bundle results in the finger exhibiting larger relative resistance shifts since a larger deformation is allowed. The curve of glass is the same as that of the ice cube, so the two curves almost overlap with each other. Nevertheless, when a piece of heated glass is touched (150 °C), the relative resistance of the finger varies more than that when a piece of glass at room temperature is touched, which occurs because the high temperature also increases the deformation of the ETSA, as demonstrated in Fig. 4f. In addition to increased relative resistance changes, the colour of the fingertip shifted from tea green to orange-red when it touched the heated glass, providing a visual warning for touching high-temperature objects. Fig. 5e depicts a walking, colourful inchworm composed of a U-shaped ETSA that can walk under periodic electrical stimuli. When powered on, due to the electrothermal effect, the rear leg deforms and slides forward. To prevent the rear leg from slipping back, two pointed feet were assembled to the rear leg to increase the friction between the rear leg and the ground. When powered off, the feet would be blocked by the rough ground; thus, the inchworm can still "walk" forward (Fig. S6, Supporting Information). As a result, the repeated bending and extension motions of the two legs can be converted into a forward motion of the inchworm. The proposed inchworm can crawl 30 mm in 360 s (Movie S3, Supporting Information). In addition, the relative resistance of the inchworm decreases or increases repeatedly during the crawling process, and the colour of the inchworm also changes correspondingly. From this electrical and visual signal feedback, we can monitor the motion state of the inchworm in real time through output electrical resistance and thermochromic colour changes.

Supplementary video related to this article can be found at https://doi.org/10.1016/j.nanoen.2020.104926

To demonstrate the specific application of the proposed actuator, the ETSA was used in the Chinese traditional shadow play *Wu Song Fights the Tiger* as in Fig. 5f. The characters in the play are all driven by strip ETSAs (40 × 5 mm) controlled by two parallel circuits with a common power supply and switch (Fig. 5f2). When the circuit of Wu Song was connected, the ETSA mounted on the puppet drives the character to fight and kick, and then the tiger's head and tail hangs down when the switch of the tiger is pulled down (Movie S4, Supporting Information). The actuation diagrams of Wu Song and the tiger are shown in Fig. 5f3. The ends of the strip ETSA are fixed vertically to the character's torso and limbs so that the joints can move through ETSA bending, and as a result, these artificial puppets can drive themselves without human hands. More complex motions can likely be realized by the assembly of more ETSAs with appropriate circuit control.

Supplementary data related to this article can be found at https://doi.org/10.1016/j.nanoen.2020.104926.

4. Conclusions

In summary, we have developed a new kind of soft actuator integrated with real-time electrical and visual dual channel signal feedback for motion perception. The bimorph structure with cellulose paper and PI tape as passive and active layers, respectively, was used to fabricate thermally/electrothermally driven soft actuators. PDA-Zn^{2+} was adopted as a thermochromic layer deposited on the paper layer, while the M/G bilayer, with low TCR, was constructed as a conductive layer to endow actuators with effective electrothermal and electrical signal feedback. The resulting bimorph actuators have been proven to have excellent actuating performances with a large deformation curvature of 1.15 cm^{-1}, a high blocking force of 6 mN, and a long cycle life of 6000 cycles. More importantly, the suitably complementary PDA-Zn^{2+} layer and M/G bilayer eliminated the dependency on sensing components for state detection, allowing real-time sensory feedback via colour shifting and output resistance. To demonstrate the application of this device in soft robots, we integrated the proposed soft actuator into a lightweight claw, an artificial tactile finger, a walking, colourful inchworm, and a motion-programmable electro-puppetry robot for simultaneous successful actuation and perception. The proposed soft bimorph actuators with real-time multiplex motion perception exhibit much potential in soft bionic robotics and machines.

Declaration of competing interest

The authors declare that they have no known competing financial interests or personal relationships that could have appeared to influence the work reported in this paper.

CRediT authorship contribution statement

Hongtao Zhao: Data curation, Writing - original draft. **Run Hu:** Data curation, Writing - original draft. **Pan Li:** Writing - review & editing. **Anzhu Gao:** Writing - review & editing. **Xuantong Sun:** Visualization, Investigation, Validation. **Xiaohui Zhang:** Visualization, Investigation, Validation. **Xiangjun Qi:** Visualization, Investigation, Validation. **Qiang Fan:** Visualization, Investigation, Validation. **Yida Liu:** Writing - review & editing. **Xuqing Liu:** Visualization, Investigation, Validation. **Mingwei Tian:** Conceptualization, Methodology, Software, Supervision. **Guangming Tao:** Conceptualization, Methodology, Software, Supervision. **Lijun Qu:** Supervision.

Acknowledgements

We thank Z. Li for helping with the SEM measurement, K. Zhang for helping with the CIE chromaticity coordinates measurement, and we appreciated X. Hu, F. Sun for the helpful discussion. This work was supported by National Natural Science Foundation of China (61875064, 51672141, 51306095, 51606074), Natural Science Foundation of Shandong Province of China (ZR2018QEM004), Shandong Province Key Research and Development Plan (2019JZZY010340, 2019JZZY010335), Anhui Province Special Science and Technology Project (201903a05020028) and Shandong provincial universities

youth innovation technology plan innovation team (2020KJA013). H. Zhao and R. Hu contributed equally to this work.

Appendix A. Supplementary data

Supplementary data to this article can be found online at https://doi.org/10.1016/j.nanoen.2020.104926.

References

[1] E. Acome, S. Mitchell, T. Morrissey, M. Emmett, C. Benjamin, M. King, M. Radakovitz, C. Keplinger, Hydraulically amplified self-healing electrostatic actuators with muscle-like performance, Science 359 (2018) 61–65.

[2] J. Chen, F.K.-C. Leung, M.C. Stuart, T. Kajitani, T. Fukushima, E. van der Giessen, B.L. Feringa, Artificial muscle-like function from hierarchical supramolecular assembly of photoresponsive molecular motors, Nat. Chem. 10 (2018) 132–138.

[3] C.S. Haines, M.D. Lima, N. Li, G.M. Spinks, J. Foroughi, J.D. Madden, S.H. Kim, S. Fang, M.J. De Andrade, F. Göktepe, Artificial muscles from fishing line and sewing thread, Science 343 (2014) 868–872.

[4] S.M. Chin, C.V. Synatschke, S. Liu, R.J. Nap, N.A. Sather, Q. Wang, Z. Álvarez, A. N. Edelbrock, T. Fyrner, L.C. Palmer, Covalent-supramolecular hybrid polymers as muscle-inspired anisotropic actuators, Nat. Commun. 9 (2018) 2395.

[5] M. Amjadi, M. Sitti, Self-sensing paper actuators based on graphite–carbon nanotube hybrid films, Adv. Sci. 5 (2018), 1800239.

[6] S. Taccola, F. Greco, E. Sinibaldi, A. Mondini, B. Mazzolai, V. Mattoli, Toward a new generation of electrically controllable hygromorphic soft actuators, Adv. Mater. 27 (2015) 1668–1675.

[7] P. Xiao, Y. Liang, J. He, L. Zhang, S. Wang, J. Gu, J. Zhang, Y. Huang, S.-W. Kuo, T. Chen, Hydrophilic/Hydrophobic interphase-mediated bubble-like stretchable janus ultrathin films toward self-adaptive and pneumatic multifunctional electronics, ACS Nano 13 (2019) 4368–4378.

[8] W. Yan, C. Dong, Y. Xiang, S. Jiang, A. Leber, G. Loke, W. Xu, C. Hou, S. Zhou, M. Cheng, R. Hu, P. Shum, L. Wei, X. Jia, F. Sorin, X. Tao, G. Tao, Thermally drawn advanced functional fibers: new frontier of flexible electronics, Mater. Today 35 (2020) 168–194.

[9] J. Gong, H. Lin, J.W. Dunlop, J. Yuan, Hierarchically arranged helical fiber actuators derived from commercial cloth, Adv. Mater. 29 (2017), 1605103.

[10] T. Jia, Y. Wang, Y. Dou, Y. Li, M. Jung de Andrade, R. Wang, S. Fang, J. Li, Z. Yu, R. Qiao, Moisture sensitive smart yarns and textiles from self-balanced silk fiber muscles, Adv. Funct. Mater. 29 (2019), 1808241.

[11] Q. Shi, J. Li, C. Hou, Y. Shao, Q. Zhang, Y. Li, H. Wang, A remote controllable fiber-type near-infrared light-responsive actuator, Chem. Commun. 53 (2017) 11118–11121.

[12] X. Hu, M. Tian, N. Pan, B. Sun, Z. Li, Y. Ma, X. Zhang, S. Zhu, Z. Chen, L. Qu, Structure-tunable graphene oxide fibers via microfluidic spinning route for multifunctional textile, Carbon 152 (2019) 106–113.

[13] Q. Zhang, H. Li, M. Poh, F. Xia, Z.-Y. Cheng, H. Xu, C. Huang, An all-organic composite actuator material with a high dielectric constant, Nature 419 (2002) 284–287.

[14] Z. Liu, S. Fang, F.A. Moura, J. Ding, N. Jiang, J. Di, M. Zhang, X. Lepró, D. Galvao, C. Haines, Hierarchically buckled sheath-core fibers for superelastic electronics, sensors, and muscles, Science 349 (2015), 400-404-4.

[15] Y.Y. Xiao, Z.C. Jiang, X. Tong, Y. Zhao, Biomimetic locomotion of electrically powered "janus" soft robots using a liquid crystal polymer, Adv. Mater. 31 (2019), 1903452.

[16] D.D. Han, Y.L. Zhang, J.N. Ma, Y.Q. Liu, B. Han, H.B. Sun, Light-mediated manufacture and manipulation of actuators, Adv. Mater. 28 (2016) 8328–8343.

[17] W. Wang, C.X. Xiang, D. Sun, M. Li, K. Yan, D. Wang, Photothermal and moisture actuator made with graphene oxide and sodium alginate for remotely controllable and programmable intelligent devices, ACS Appl. Mater. Interfaces 11 (2019) 21926–21934.

[18] B. Han, Y.L. Zhang, L. Zhu, Y. Li, Z.C. Ma, Y.Q. Liu, X.L. Zhang, X.W. Cao, Q. D. Chen, C.W. Qiu, Plasmonic-assisted graphene oxide artificial muscles, Adv. Mater. 31 (2019), 1806386.

[19] W.A.D.M. Jayathilaka, K. Qi, Y. Qin, A. Chinnappan, W. Serrano-García, C. Baskar, H. Wang, J. He, S. Cui, S.W. Thomas, Significance of nanomaterials in wearables: a review on wearable actuators and sensors, Adv. Mater. 31 (2019), 1805921.

[20] R. Hu, S. Zhou, Y. Li, D.Y. Lei, X.B. Luo, a.W. Qiu, Illusion thermotics, Adv. Mater. 30 (2018), 1707237.

[21] R. Hu, S. Huang, M. Wang, X.B. Luo, J. Shiomi, C.W. Qiu, Encrypted thermal printing with regionalization transformation, Adv. Mater. 31 (2019), 1807849.

[22] L.X. Liu, W. Chen, H.B. Zhang, Q.W. Wang, F. Guan, Z.Z. Yu, Flexible and multifunctional silk textiles with biomimetic leaf-like MXene/silver nanowire nanostructures for electromagnetic interference shielding, humidity monitoring, and self-derived hydrophobicity, Adv. Funct. Mater. 29 (2019), 1905197.

[23] R. Castaldo, G.C. Lama, P. Aprea, G. Gentile, V. Ambrogi, M. Lavorgna, P. Cerruti, Humidity-driven mechanical and electrical response of graphene/cloisite hybrid films, Adv. Funct. Mater. 29 (2019), 1807744.

[24] D.D. Han, Y.L. Zhang, H.B. Jiang, H. Xia, J. Feng, Q.D. Chen, H.L. Xu, H.B. Sun, Moisture-responsive graphene paper prepared by self-controlled photoreduction, Adv. Mater. 27 (2015) 332–338.

[25] C. Zhang, J. Wang, W. Wang, N. Xi, Y. Wang, L. Liu, Modeling and analysis of bio-syncretic micro-swimmers for cardiomyocyte-based actuation, Bioinspiration Biomimetics 11 (2016), 056006.

[26] K. Li, T.H. Chang, Q. Xie, Y. Cheng, H. Yang, J. Chen, P.Y. Chen, Tunable magnetic response in 2D materials via reversible intercalation of paramagnetic ions, Adv. Electron. Mater. 5 (2019), 1900040.

[27] G.A. Sotiriou, C.O. Blattmann, S.E. Pratsinis, Flexible, multifunctional, magnetically actuated nanocomposite films, Adv. Funct. Mater. 23 (2013) 34–41.

[28] L. Chen, M. Weng, P. Zhou, F. Huang, C. Liu, S. Fan, W. Zhang, Graphene-based actuator with integrated-sensing function, Adv. Funct. Mater. 29 (2019), 1806057.

[29] K. Chu, S.-C. Lee, S. Lee, D. Kim, C. Moon, S.H. Park, Smart conducting polymer composites having zero temperature coefficient of resistance, Nanoscale 7 (2015) 471–478.

[30] B. Fang, J. Xi, Y. Liu, F. Guo, Z. Xu, W. Gao, D. Guo, P. Li, C. Gao, Wrinkle-stabilized metal-graphene hybrid fibers with zero temperature coefficient of resistance, Nanoscale 9 (2017) 12178–12188.

[31] W. He, G. Li, S. Zhang, Y. Wei, J. Wang, Q. Li, X. Zhang, Polypyrrole/silver coaxial nanowire aero-sponges for temperature-independent stress sensing and stress-triggered joule heating, ACS Nano 9 (2015) 4244–4251.

[32] K. Li, Y. Shao, H. Yan, Z. Lu, K.J. Griffith, J. Yan, G. Wang, H. Fan, J. Lu, W. Huang, Lattice-contraction triggered synchronous electrochromic actuator, Nat. Commun. 9 (2018) 4798.

[33] M. Dharmarwardana, R.P. Welch, S. Kwon, V.K. Nguyen, G.T. McCandless, M. A. Omary, J.J. Gassensmith, Thermo-mechanically responsive crystalline organic cantilever, Chem. Commun. 53 (2017) 9890–9893.

[34] B. Zuo, M. Wang, B.-P. Lin, H. Yang, Photomodulated tricolor-changing artificial flowers, Chem. Mater. 30 (2018) 8079–8088.

[35] H. Zhao, M. Tian, Z. Li, Y. Zhang, S. Zhu, X. Zhang, S. Chen, L. Qu, Enhanced electrical conductivity of silver nanoparticles decorated fabrics with sandwich micro-structure coating layer based on "silver colloid effect", Mater. Lett. 240 (2019) 5–8.

[36] H. Zhao, M. Tian, Z. Li, Y. Zhang, Z. Chen, W. Zhang, S. Zhu, Y. Sun, Z. Zhou, L. Qu, Robust sandwich micro-structure coating layer for wear-resistant conductive polyester fabrics, Appl. Surf. Sci. 494 (2019) 969–976.

[37] M. Okaniwa, Y. Oaki, S. Kaneko, K. Ishida, H. Maki, H. Imai, Advanced biomimetic approach for crystal growth in nonaqueous media: morphology and orientation control of pentacosadiynoic acid and applications, Chem. Mater. 27 (2015) 2627–2632.

[38] S.M. Mirvakili, I.W. Hunter, Multidirectional artificial muscles from nylon, Adv. Mater. 29 (2017), 1604734.

[39] K. Hantanasirisakul, Y. Gogotsi, Electronic and optical properties of 2D transition metal carbides and nitrides (MXenes), Adv. Mater. 30 (2018), 1804779.

[40] B. Fang, J. Xi, Y. Liu, F. Guo, Z. Xu, W. Gao, D. Guo, P. Li, C. Gao, Wrinkle-stabilized metal-graphene hybrid fibers with zero temperature coefficient of resistance, Nanoscale 9 (2017) 12178–12188.

[41] H. Zhao, M. Tian, Y. Hao, L. Qu, S. Zhu, S. Chen, Fast and facile graphene oxide grafting on hydrophobic polyamide fabric via electrophoretic deposition route, J. Mater. Sci. 53 (2018) 9504–9520.

[42] Y. Hao, M. Tian, H. Zhao, L. Qu, S. Zhu, X. Zhang, S. Chen, K. Wang, J. Ran, High efficiency electrothermal graphene/tourmaline composite fabric joule heater with durable abrasion resistance via a spray coating route, Ind. Eng. Chem. Res. 57 (2018) 13437–13448.

[43] M. Tian, Y. Hao, L. Qu, S. Zhu, X. Zhang, S. Chen, Enhanced electrothermal efficiency of flexible graphene fabric Joule heaters with the aid of graphene oxide, Mater. Lett. 234 (2019) 101–104.

[44] M. Naguib, V.N. Mochalin, M.W. Barsoum, Y. Gogotsi, 25th anniversary article: MXenes: a new family of two-dimensional materials, Adv. Mater. 26 (2014) 992–1005.

[45] T.H. Park, S. Yu, M. Koo, H. Kim, E.H. Kim, J.-E. Park, B. Ok, B. Kim, S.H. Noh, C. Park, Shape-adaptable 2D titanium carbide (MXene) heater, ACS Nano 13 (2019) 6835–6844.

[46] F. Sun, M. Tian, X. Sun, T. Xu, X. Liu, S. Zhu, X. Zhang, L. Qu, Stretchable conductive fibers of ultrahigh tensile strain and stable conductance enabled by a worm-shaped graphene microlayer, Nano Lett. 19 (2019) 6592–6599.

[47] M. Tian, R. Zhao, L. Qu, Z. Chen, S. Chen, S. Zhu, W. Song, X. Zhang, Y. Sun, R. Fu, Stretchable and designable textile pattern strain sensors based on graphene decorated conductive nylon filaments, Macromol. Mater. Eng. 304 (2019), 1900244.

[48] Y. Lu, M. Tian, X. Sun, N. Pan, F. Chen, S. Zhu, X. Zhang, S. Chen, Highly sensitive wearable 3D piezoresistive pressure sensors based on graphene coated isotropic non-woven substrate, Compos. Part A-appl. S. 117 (2019) 202–210.